ENGINEERING

3D bioprinting spatiotemporally defined patterns of growth factors to tightly control tissue regeneration

Fiona E. Freeman[1,2], Pierluca Pitacco[1,2], Lieke H. A. van Dommelen[3], Jessica Nulty[1,2], David C. Browe[1,2], Jung-Youn Shin[4], Eben Alsberg[4,5], Daniel J. Kelly[1,2,6,7]*

Therapeutic growth factor delivery typically requires supraphysiological dosages, which can cause undesirable off-target effects. The aim of this study was to 3D bioprint implants containing spatiotemporally defined patterns of growth factors optimized for coupled angiogenesis and osteogenesis. Using nanoparticle functionalized bioinks, it was possible to print implants with distinct growth factor patterns and release profiles spanning from days to weeks. The extent of angiogenesis in vivo depended on the spatial presentation of vascular endothelial growth factor (VEGF). Higher levels of vessel invasion were observed in implants containing a spatial gradient of VEGF compared to those homogenously loaded with the same total amount of protein. Printed implants containing a gradient of VEGF, coupled with spatially defined BMP-2 localization and release kinetics, accelerated large bone defect healing with little heterotopic bone formation. This demonstrates the potential of growth factor printing, a putative point of care therapy, for tightly controlled tissue regeneration.

INTRODUCTION

In recent years, a number of growth factors have been tested in clinical trials for a variety of therapeutic applications including bone regeneration and neovascularization of ischemic tissues. Despite early promising results, the results obtained in larger phase 2 trials have often not shown the expected benefit to patients (*1*, *2*), with some having marked adverse effects (*3*–*5*). The Infuse bone graft, which consists of recombinant human bone morphogenetic protein-2 (rhBMP-2) soaked onto a collagen sponge at a dosage of 1.5 mg/ml, has received Food and Drug Administration approval for certain spinal, dental, and trauma indications and is in widespread clinical use. However, major complications and adverse effects have increasingly been attributed because of the "off-label" use of the product (*3*, *4*). Clinically, the current delivery vehicle for BMP-2 is a collagen powder or sponge that has been shown to result in a large initial burst release, which contrasts with the expression profile observed during normal fracture repair where BMP expression increases until day 21, suggesting a need for slower and more sustained growth factor release profile (*6*, *7*). Furthermore, because of the short half-life of the growth factor and the harsh fracture environment (*5*), supraphysiological dosages of BMP-2 are being delivered to elicit bone regeneration, which has been linked to adverse effects such as heterotopic ossification. Therefore, there is a clear clinical need to develop alternative strategies to deliver single or multiple growth factors to the site of injury with sustainable and physiologically relevant dosages such that repair is induced without these adverse effects.

A number of growth factors have been shown to be expressed at different phases of fracture healing, including vascular endothelial growth factor (VEGF) and BMPs. The coupled relationship in bone healing, both physical and biochemical, between blood vessels and bone cells has long been recognized (*8*, *9*). During fracture healing, VEGF is released directly after injury and predominately drives the formation of the fracture hematoma (*9*). Inhibition of VEGF has been shown to disrupt the repair of fractures and large bone defects (*10*–*12*). Despite this, VEGF delivery alone is often not sufficient to heal critically sized bone defects, which may be due to suboptimal dosing or the timing of VEGF release. Furthermore, VEGF does not appear to drive progenitor cell differentiation toward the chondrogenic or osteogenic lineage; therefore, combination therapies with BMPs have been developed in an attempt to accelerate the regeneration of large bone defects (*9*, *13*–*18*). During normal fracture healing, VEGF expression peaks around day 5/10 (*19*, *20*) and then decreases, whereas BMP-2 expression increases constantly until day 21, suggesting a need for delivery systems that support the early release of VEGF and the sustained release of BMP-2 (*6*, *7*, *19*, *20*). To this end, composite polymer systems have been used to deliver VEGF and BMP-2 in a sequential fashion (*15*–*18*). The timed release of VEGF/BMP-2 was found to enhance ectopic bone formation (*16*–*18*); however, in an orthotopic defect, no significant benefit was observed (*17*, *18*). This may be due to the high dose of VEGF used in these studies (*18*), which has previously been shown to disrupt osteogenesis as a result of abnormal angiogenesis and vascular structure (*8*), or due to suboptimal growth factor release profiles from these constructs. This suggests that novel strategies are required for delivering low-dosage VEGF and BMP-2, with tight temporal control, to enhance vascularization and subsequent bone formation in orthotopic defects. Nanoparticles such as hydroxyapatite (HA) and laponite are known to be osteoinductive and have previously been shown to facilitate the adsorption and immobilization of proteins such as VEGF and BMP-2 because of the strong attraction between the nanoparticles and the growth factor (*21*–*23*). This motivates the integration of these nanoparticles into regenerative implants to enable tight temporal control over the rate at which encapsulated growth factors are released into damaged tissue.

[1]Trinity Centre for Biomedical Engineering, Trinity Biomedical Sciences Institute, Trinity College Dublin, Ireland. [2]Department of Mechanical and Manufacturing Engineering, School of Engineering, Trinity College Dublin, Ireland. [3]Orthopaedic Biomechanics, Department of Biomedical Engineering, Eindhoven University of Technology, P.O. Box 513, 5600 MB Eindhoven, The Netherlands. [4]Departments of Biomedical Engineering and Orthopaedic Surgery, Case Western Reserve University, Cleveland, OH 44106, USA. [5]Departments of Biomedical Engineering, Pharmacology, Orthopaedics, and Mechanical and Industrial Engineering, University of Illinois at Chicago, Chicago, IL 60607, USA. [6]Department of Anatomy, Royal College of Surgeons in Ireland, Dublin, Ireland. [7]Advanced Materials and Bioengineering Research Centre (AMBER), Royal College of Surgeons in Ireland and Trinity College Dublin, Dublin, Ireland.
*Corresponding author. Email: kellyd9@tcd.ie

Processes such as angiogenesis are regulated not only by the temporal presentation of growth factors but also by spatial gradients of morphogens that regulate chemotactic cell migration. Using microfluidic devices (*24*, *25*) or three-dimensional (3D) culture models (*26*, *27*), it has been demonstrated that endothelial cell migration is mediated by gradients in VEGF. However, it is unclear whether incorporating gradients of VEGF into tissue-engineered scaffolds will enhance angiogenesis in vivo. Here, we used emerging multiple-tool biofabrication techniques (*28*) to deliver VEGF and BMP-2 with distinct spatiotemporal release profiles to enhance the regeneration of critically sized bone defects. To tune the temporal release of these morphogens from 3D printed constructs, we functionalized alginate-based bioinks with different nanoparticles known to bind these regulatory factors. Both the spatial position and temporal release of growth factor from the 3D printed implant determined its therapeutic potential. By slowing the release of BMP-2, it was possible to enhance bone formation in vivo within predefined positions of the implant. Furthermore, introducing spatial gradients of VEGF into 3D printed implants enhanced vascularization in vivo compared to controls homogenously loaded with the same total amount of growth factor. We also demonstrate accelerated large bone defect healing, with minimal ectopic bone formation, using 3D printed implants containing a spatial gradient of VEGF and spatially localized BMP-2.

RESULTS

Development of bioinks with temporally distinct growth factor release profiles

To produce a printable bioink, various weight concentrations of methylcellulose were first added to RGD γ-irradiated alginate. Print fidelity (as measured by the filament spreading ratio) improved by increasing the methylcellulose content [see fig. S1 (A and B)]; however, the capacity to print multiple layers of material worsens because of the overly adhesive nature of the ink. For these reasons, a weight concentration of 2:1 (w/w) alginate to methylcellulose was chosen for all bioinks, as it substantially increased the print fidelity while allowing multiple layers of material to be accurately deposited.

To tune the temporal release profile of growth factor (here, VEGF), clay nanoparticles (*22*, *23*, *29*) or hydroxyapatite nanoparticles (nHA) (*21*) were added to the alginate-methylcellulose bioink. Adding methylcellulose to the alginate to produce a printable ink significantly increased the release of VEGF compared to that observed from alginate only [see fig. S1 (C and D)]. The addition of laponite, a clay-based nanoparticle, markedly slowed the release of VEGF (see fig. S1C), while the incorporation of nHA only had a small effect on growth factor release, producing a slightly more gradual release profile (see fig. S1D). This blend (alginate, methylcellulose, and nHA) will hereafter be referred to as the vascular bioink, as it allowed for the near complete release of VEGF over 10 days, mimicking that observed during normal fracture healing (*19*, *20*). No laponite was included in this vascular bioink.

To demonstrate the utility of this vascular bioink, two strategies were compared to print implants containing a spatial gradient of VEGF (see fig. S1E). In the first, VEGF (100 ng/ml) was printed into the central 5-mm core of constructs 8 mm in diameter and 4 mm high, with a VEGF-free bioink used to print the periphery of the construct. In the second, VEGF (80 ng/ml) was printed into the center of the construct, and VEGF (20 ng/ml) was printed around the periphery of the implant. Control constructs containing a homogenous distribution of VEGF were also printed. One hour after printing, clear spatial differences in VEGF localization were observed in both gradient constructs, while roughly the same amount of protein was detected in the core and periphery of the homogenous VEGF control (see fig. S1F). Fourteen days after printing, a spatial gradient still existed in the construct that initially had all VEGF loaded into its central region, with no gradient observed in the other groups (see fig. S1G). This demonstrates that spatial gradients of growth factor can be maintained within constructs for at least 14 days after printing.

Printed VEGF gradients enhance angiogenesis in vivo

We next sought to assess whether depositing spatial gradients of VEGF within 3D printed polycaprolactone (PCL) implants would accelerate vascularization of the constructs in vivo. To this end, Homogenous VEGF, Gradient VEGF, and No VEGF constructs were implanted subcutaneously in the back of mice (see Fig. 1A), where the total amount of growth factor (25 ng) within the two VEGF-containing implants was constant. Two weeks after implantation, histological analysis of hematoxylin and eosin (H&E)–stained samples revealed the presence of vessels in the Homogenous VEGF and Gradient VEGF groups; however, there were no obvious vessels present in the No VEGF group (see Fig. 1B). These vessels appeared mature, complete with α–smooth muscle actin (α-SMA) and von Willebrand factor (vWF)–stained walls and perfused with erythrocytes (see fig. S2A). The Homogenous VEGF constructs had vessels predominantly located in the periphery of the scaffold, with little to none present within the center of the scaffold. On the other hand, vessels were present both in the periphery and in the center of the Gradient VEGF group. Four weeks after implantation, all three experimental groups had mature vessels present (see Fig. 1C and fig. S2B). Similar to the Homogeneous VEGF group, the No VEGF group had vessels predominantly located in the periphery of the constructs, with little to none present within the center of the construct. When quantified, at both 2 and 4 weeks, there were significantly more vessels present in the Gradient VEGF group compared to both the Homogenous VEGF and No VEGF group (see Fig. 1D). There was significantly more vessels present in the periphery of the Gradient VEGF constructs at both 2 and 4 weeks in vivo compared to the other two experimental groups [see Fig. 1 (E and F)]. There was also a trend toward a larger number of vessels present in the center of the Gradient VEGF construct at 4 weeks compared to No VEGF ($P = 0.09$) and Homogenous VEGF ($P = 0.1$) groups (see Fig. 1F).

Spatiotemporal delivery of BMP-2 to localize bone formation in vivo

Recognizing that a slower and more sustained release of BMP-2 could be beneficial for promoting osteogenesis (*6*, *7*), we next sought to compare bone formation in vivo within implants with temporally distinct growth factor release profiles. To the base alginate-methylcellulose bioink (here termed the Fast BMP-2 Release bioink), laponite at varying w/w ratios of laponite to alginate were compared to determine the optimum ratio to generate a Slow BMP-2 Release bioink (see fig. S3). As there was little difference in the growth factor release profile from the different groups, a 6:1 alginate:laponite w/w ratio was chosen to minimize the amount of laponite in the bioink. The addition of laponite markedly slowed the in vitro release of BMP-2 from the bioink, resulting in a reasonable constant release of growth factor from day 7 to day 35 (see Fig. 2C).

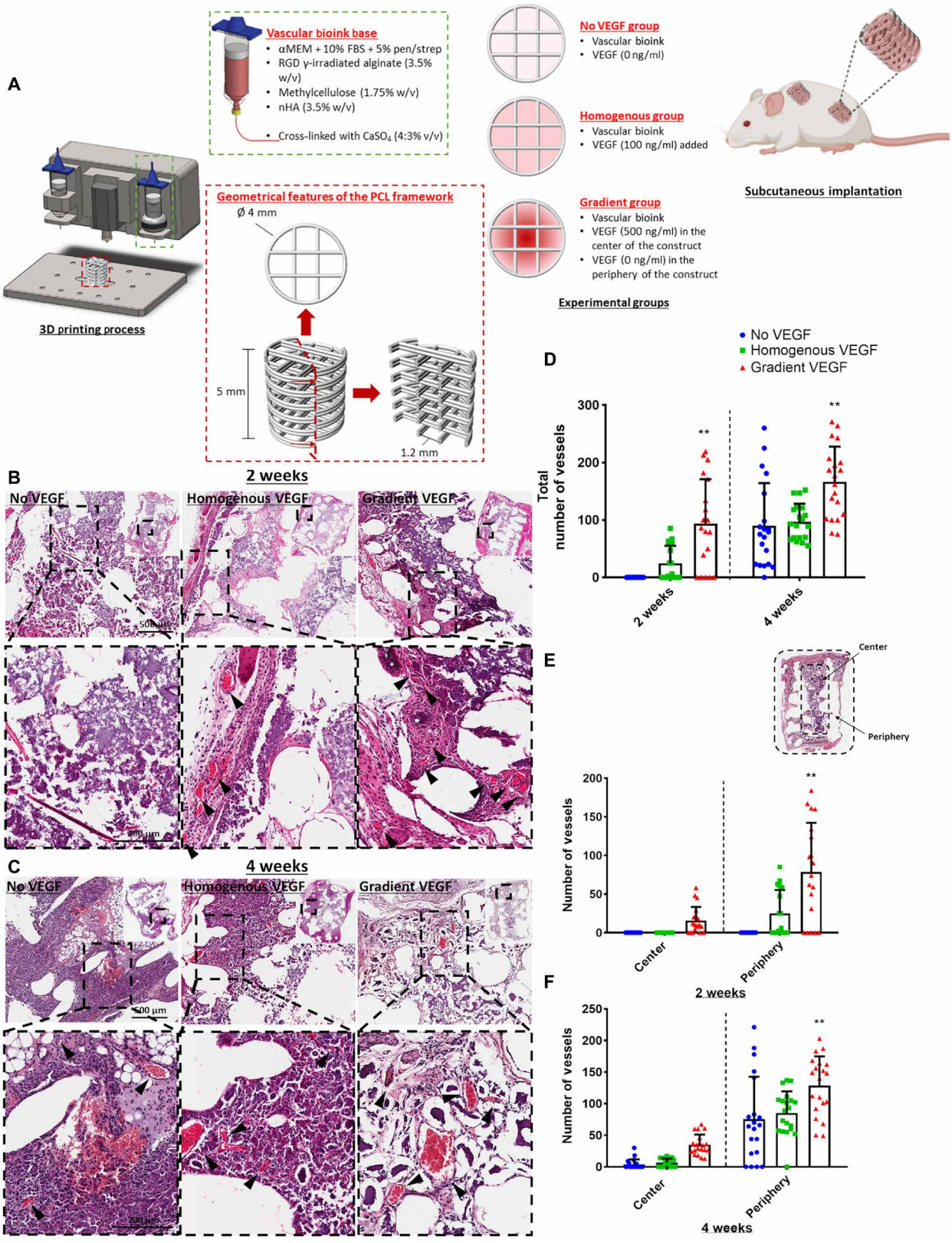

Fig. 1. Enhanced vessel infiltration and angiogenesis due to distinct VEGF gradient. (**A**) Schematic of the 3D printed scaffold and experimental groups. Construct design (4 mm in diameter, 5 mm in height). H&E-stained sections of the three experimental groups at (**B**) 2 and (**C**) 4 weeks in vivo. Images were taken at 20×. Arrows denote vessels. (**D**) Total number of vessels of the experimental groups at 2 and 4 weeks in vivo. Number of vessels present in the center versus the periphery at (**E**) 2 and (**F**) 4 weeks in vivo. $^{**}P < 0.01$. Error bars denote SDs ($n = 8$ animals; $n = 5$ slices per animal). FBS, fetal bovine serum; pen/strep, penicillin/streptomycin.

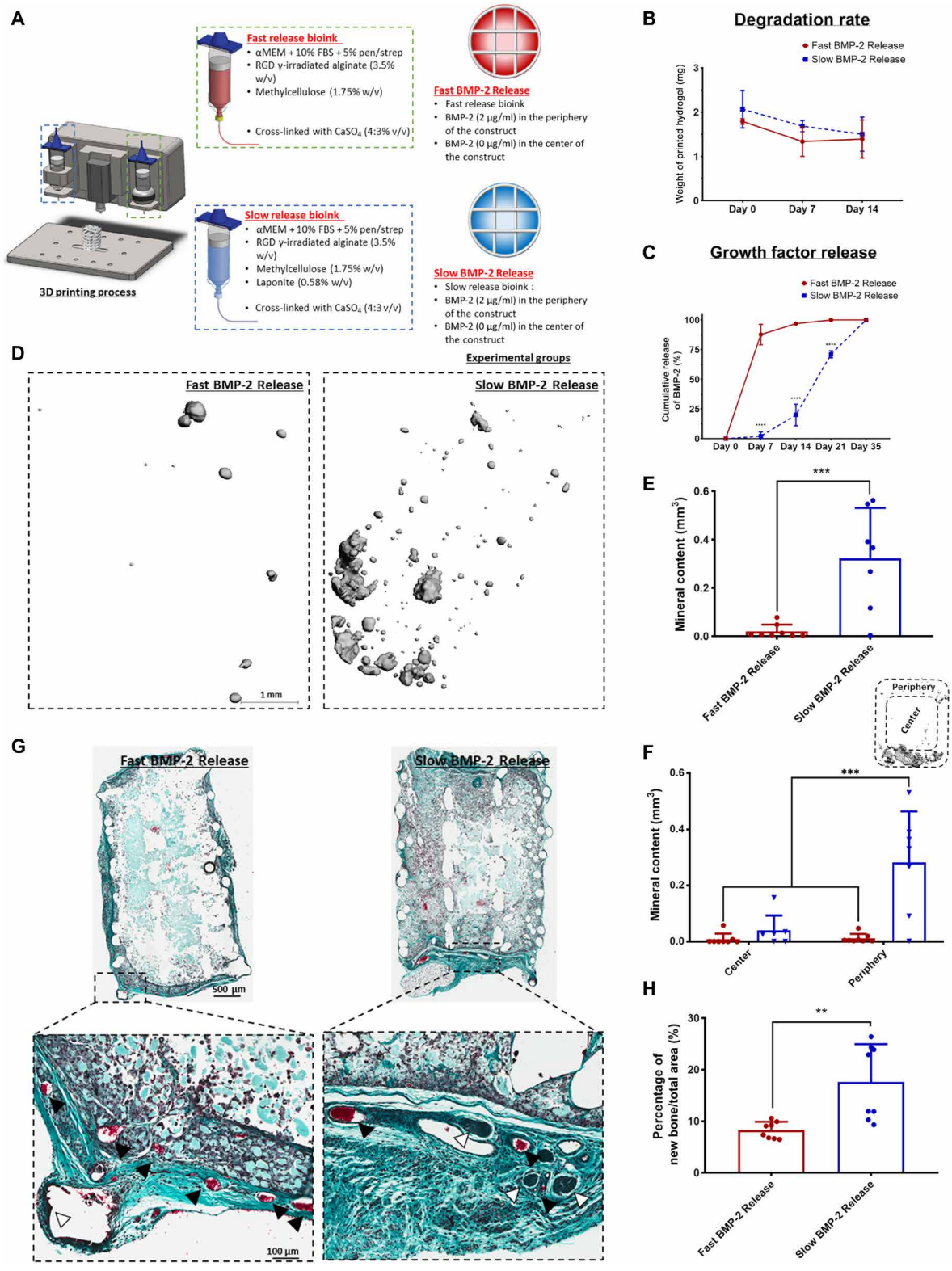

Fig. 2. Localized-temporal delivery of BMP-2 led to controlled bone formation. (**A**) Schematic of the experimental groups. Construct design (4 mm in diameter, 5 mm in height). αMEM, alpha minimum essential medium. (**B**) Degradation of the two bioinks. (**C**) Cumulative release of BMP-2 of the fast release bioink versus the slow release bioink. (**D**) 3D reconstructions of the μCT data for each group at 8 weeks. (**E**) μCT analysis on total mineral deposition of each of the groups after 8 weeks in vivo. (**F**) μCT analysis on the location of mineral deposition of each of the groups after 8 weeks in vivo. ***$P < 0.001$; error bars denote SDs ($n = 8$ animals). (**G**) Goldner's trichrome–stained sections of both groups after 8 weeks in vivo. Images were taken at 20×. White arrows denote developing bone tissue, and black arrows denote blood vessels. (**H**) Quantification of the amount of new bone formation per total area. Error bars denote SDs; **$P < 0.01$ ($n = 8$ animals, $n = 6$ slices per animal).

The addition of laponite also had no significant effect on the degradation rate of the bioink (Fig. 2B).

To assess whether slow and sustained release of BMP-2 would enhance ectopic bone formation in vivo, Fast BMP-2 Release (−laponite) and Slow BMP-2 Release (+laponite) bioinks were mixed with bone marrow–derived mesenchymal stem cells (BMSCs), deposited within 3D printed scaffolds, and then implanted subcutaneously in the back of mice (see Fig. 2A). Seeding these bioinks with MSCs was used to test their potential for promoting osteogenesis in an ectopic location. BMP-2 was specifically localized around the periphery of the implant. This pattern of growth factor presentation was chosen to test the capacity of the printed implants to spatially localize bone formation in vivo (note that the geometry of the implant is the same as that which will be used in the segmental defect study below, with the BMP-2 localized to the periphery of the implant such that bone would only form along the cortical shaft of the damaged limb rather than throughout). Eight weeks after implantation, there was significantly more mineral within the Slow BMP-2 Release group compared to the Fast BMP-2 Release group [see Fig. 2 (D and E)]. Micro–computed tomography (μCT) reconstructions revealed that the mineral was preferentially deposited around the periphery of the constructs where the BMP-2 was localized [see Fig. 2 (D and F)]. Histological staining further verified this finding, with positive staining for new bone seen predominantly in the periphery of both groups (see Fig. 2G, denoted by white arrows). Quantification revealed that the Slow BMP-2 Release constructs had significantly more new bone formation per total area of construct (see Fig. 2H).

Spatiotemporal delivery of VEGF and BMP-2 enhances angiogenesis within large bone defects

We next sought to assess whether the delayed release of BMP-2 from printed constructs containing spatial gradients in VEGF would enhance angiogenesis and bone formation within critically sized bone defects. To this end, VEGF gradient only, BMP-2 gradient only, and Composite (VEGF+BMP-2 gradient) constructs were printed and implanted in a 5-mm rat femoral defect (see Fig. 3A) and compared to an empty defect.

Two weeks after implantation, μCT angiography was used to quantify and visualize the early vascular network that had formed within the defect site. 3D reconstructions revealed that vascular networks had formed in all four experimental groups (see Fig. 3B). When quantified, there was a significant increase in vessel volume in the Composite group compared to the VEGF gradient group (see Fig. 3C). There was also a significant increase in average vessel thickness in the BMP-2 gradient and Composite groups compared to the VEGF gradient group (see Fig. 3D). Although there was no significant difference in the connectivity of the vessels, there was a trend ($P = 0.1$) toward increased connectivity in the Composite group compared to the VEGF gradient group (see Fig. 3E). 3D reconstructions also revealed the presence of primitive immature blood vessels depicted by large globules of contrast agent (denoted by the red arrows in Fig. 3B). There appeared to be fewer primitive blood vessels present in the Composite group than the other three experimental groups. This was further verified by α–SMA and vWF staining, which revealed a larger number of vessels with only positive vWF-stained walls in the Empty and VEGF gradient groups (see Fig. 3F, denoted by white arrows). On the other hand, there were predominately more mature vessels with α–SMA and vWF-stained walls in both the BMP-2 gradient and Composite groups (see Fig. 3F, denoted by yellow arrows). Note that the differences in angiogenesis seen between the VEGF gradient and Composite groups (same amount of VEGF in both groups) could at least partially be explained by looking at the VEGF release profile from both groups (see fig. S4). The addition of the osteoinductive ink around the implant periphery significantly reduced the VEGF release rate from construct into the media, with a more linear release of growth factor over time.

Accelerated regeneration with minimal heterotopic bone formation

Two weeks after surgery, defects within the Empty group were filled with a fibrous tissue (see Fig. 4A). In contrast, positive staining for cartilage and new bone deposition was observed in the BMP-2 gradient and Composite groups, suggesting that new bone was forming at least partially via endochondral ossification. When quantified, there was a trend toward increased cartilage development (red staining in Safranin O images) in both the BMP-2 gradient ($P = 0.12$) and Composite ($P = 0.18$) groups compared to the Empty (see Fig. 4B). No significant differences in bone formation was observed between any of the groups at week 2; however, the μCT reconstructions showed mineralized calluses beginning to form in the BMP-2 gradient and Composite groups, which was less evident in the Empty and VEGF gradient groups [see Fig. 4 (C and D)].

Next, μCT analysis was used to visualize and quantify bone formation within the defects at 4, 8, 10, and 12 weeks after implantation. Compared to the Empty group, there were significantly higher levels of new bone formation in the Composite group as early as 8 weeks after implantation [see Fig. 5 (A and B)]. A consistent pattern of healing was observed in the Composite group, with bone forming down through the PCL scaffold framework (see Fig. 5A and fig. S5). After 10 weeks of implantation, significantly higher levels of bone formation was observed in the BMP-2 gradient and Composite groups compared to the Empty group. By 12 weeks, all three experimental groups contained significantly higher levels of new bone compared to the Empty group. Twelve weeks after implantation, bone density mapping revealed that the new bone formed in the experimental groups consisted of a dense cortical-like bone present around the periphery of defect, comparable to the adjacent native bone (1200 mg HA/cm^3) (see Fig. 5C). Quantitative densitometry analysis revealed no significant difference in the average density (mg HA/cm^3) of the new bone that did form between any of the groups over the 12 weeks (see Fig. 5D).

To assess the levels of heterotopic bone formation, region of interest (ROI) bone volume analysis was performed on the week 12 reconstructions. The total bone volume was quantified in the core, annulus, and heterotopic regions of the defect (see Fig. 5E). In all three experimental groups, bone preferentially formed in the annulus of the defect, with little ectopic bone formation (see Fig. 5F). All three experimental groups had significantly higher total bone volume in the annulus of the defect compared to the Empty annulus, with the highest total bone volume present in the Composite group.

We next sought to assess the nature of new bone tissue being formed using histological staining. Goldner's trichrome staining revealed predominantly fibrous tissue formation, similar to what was seen previously at 2 weeks, in the Empty group (see Fig. 6A). There was positive staining for new bone, complete with marrow cavities, in all three experimental groups at 12 weeks after implantation. When quantified, there was significantly more bone found in all three experimental groups compared to the Empty group (see Fig. 6B). There

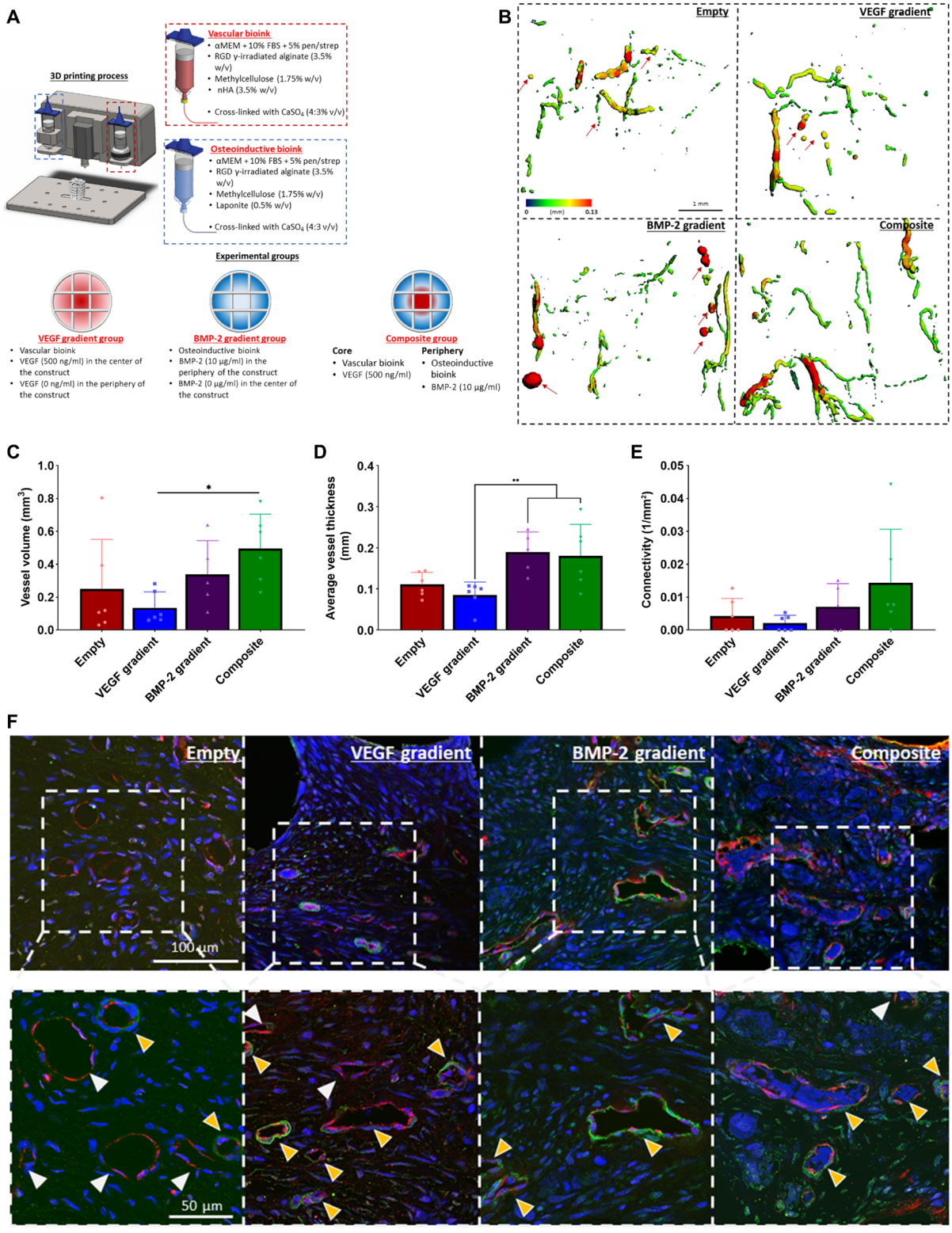

Fig. 3. Spatiotemporal delivery of both VEGF and BMP-2 led to enhanced angiogenesis. (**A**) Schematic of the 3D printed experimental groups including key features of the developed bioinks and the segmental defect procedure. Construct design (4 mm in diameter, 5 mm in height). (**B**) μCT angiography representative images of vessel diameter. Red arrows denote leaky blood vessels denoted by pools of contrast agent. Quantification on (**C**) total vessel volume, (**D**) average vessel diameter, and (**E**) connectivity for all groups after 2 weeks in vivo. *$P < 0.05$ and **$P < 0.01$; error bars denote SDs ($n = 9$ animals). (**F**) Immunohistochemical staining of nuclei (blue), vWF (red), and α–SMA (green) of the experimental groups at 2 weeks after implantation. Images were taken at 40× and 63×. Yellow arrows denote vessels with α–SMA and vWF dual staining; white arrows denote slightly less mature vessels with only vWF positive staining.

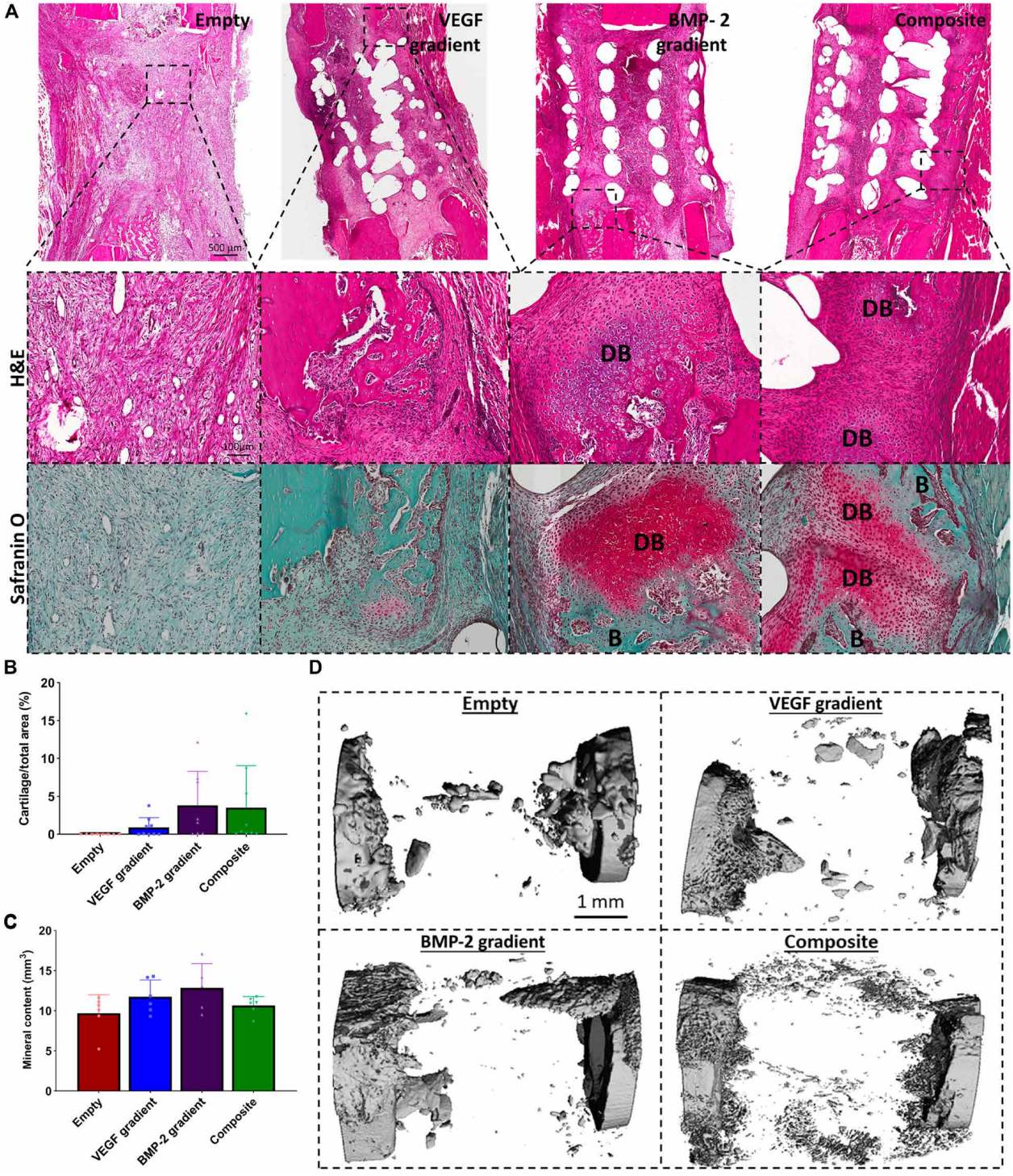

Fig. 4. Temporal delivery of exogenous BMP-2 induces early bone healing via an endochondral ossification process. (**A**) H&E- and Safranin O–stained sections of all groups after 2 weeks in vivo. Images were taken at 20×. DB denotes cartilage undergoing endochondral ossification to become developing bone, and B denotes positive new bone tissue. Quantification of the amount of (**B**) bone formation and (**C**) developing bone per total area. Error bars denote SDs ($n = 9$ animals). (**D**) μCT reconstructed images of the defect site.

were also significantly higher amounts of bone marrow present in the Composite group compared to the Empty group (see Fig. 6C). As observed in the μCT 3D reconstructions, it is clear that the bone is forming down through the PCL scaffold framework, specifically in the Composite group. Safranin O staining revealed the presence of cartilage in all three experimental groups after 12 weeks, demonstrating that bone is continuing to develop via endochondral ossification. When quantified, there was significantly more cartilage present in the Composite group compared to all other groups at this time point (see Fig. 6D).

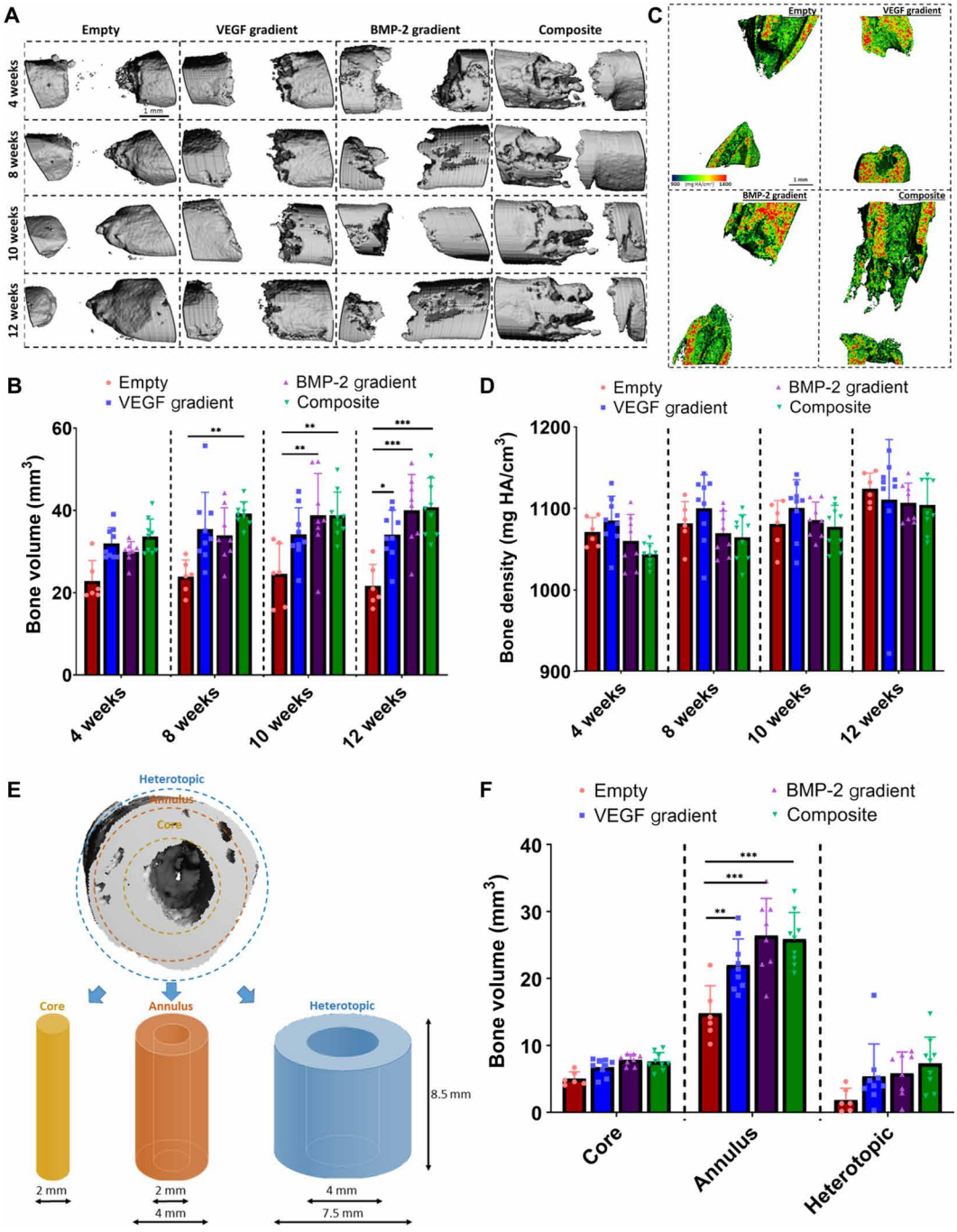

Fig. 5. Spatiotemporal delivery of both VEGF and BMP-2 led to enhanced bone tissue distribution 12 weeks after scaffold implantation. (**A**) Reconstructed in vivo μCT analysis of bone formation in the defects. (**B**) Quantification of total bone volume (mm^3) in the defects at each time point. (**C**) Representative images of μCT bone densities in the defects at 12 weeks halfway through the defect (scale bar, 1 mm throughout). (**D**) Average bone density (mg HA/cm^3) in the defects at each time point. (**E**) Outline of ROI bone volume analysis including definitions of core, annulus, and heterotopic regions. (**F**) Total bone volume (mm^3) in each region at 12 weeks. $^{**}P < 0.01$, $^{***}P < 0.001$, and $^{****}P < 0.0001$; error bars denote SDs ($n = 9$ animals).

DISCUSSION

Despite the tremendous potential of growth factor delivery, the results obtained in larger clinical trials have not always shown the expected benefit to patients (*2*), with some studies reporting marked adverse effects (*3*–*5*). The reasons for this are multifaceted, from the delivery methods to the supraphysiological dosages needed to elicit a therapeutic effect and the costs and adverse effects attached to these high doses. This study presents a novel alternative approach for spatiotemporally controlled delivery of growth factors. We developed a range of nanoparticle-functionalized bioinks to precisely control the temporal release of growth factors from 3D printed implants. Using multiple tool biofabrication techniques, we were able

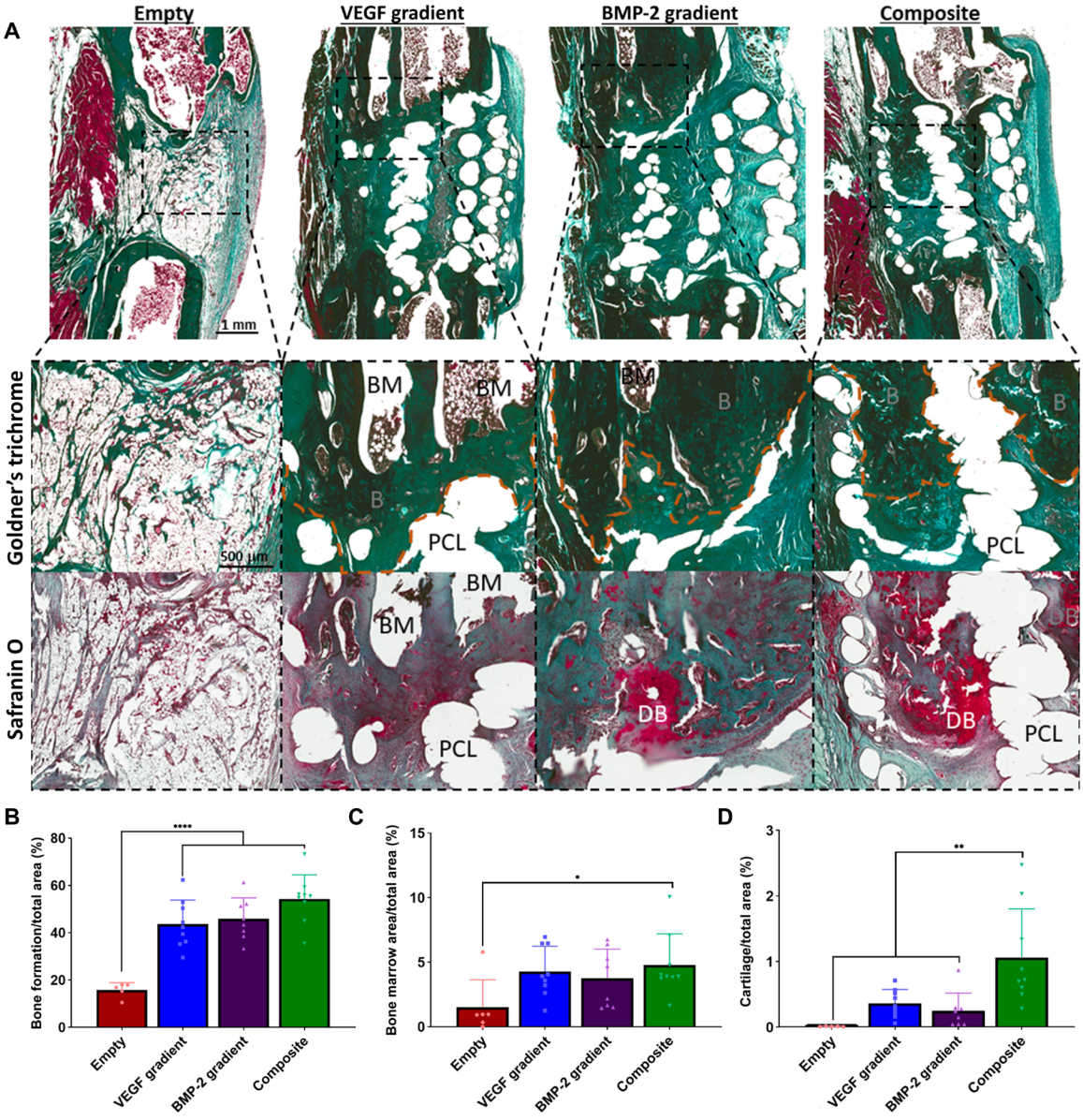

Fig. 6. Spatiotemporal delivery of both VEGF and BMP-2 led to enhanced bone healing and tissue morphology 12 weeks after scaffold implantation. (**A**) Goldner's trichrome– and Safranin O–stained sections of all groups after 12 weeks in vivo. Images were taken at 20×. BM denotes bone marrow. PCL denotes areas where the PCL frame was. DB denotes cartilage undergoing endochondral ossification to become new bone, and B denotes positive bone tissue. Quantification of the amount of (**B**) bone formation, (**C**) bone marrow, and (**D**) developing bone per total area. Error bars denote SDs. *$P < 0.05$, **$P < 0.01$, and ****$P < 0.0001$ ($n = 9$ animals).

to print constructs containing spatiotemporal gradients of growth factors, which allowed for controlled tissue regeneration without the need for supraphysiological dosages. Specifically, the appropriate patterning of VEGF enhanced angiogenesis in vivo and, when coupled with defined BMP-2 localization and release kinetics, enhanced large bone defect healing with little heterotopic bone formation.

Alginate hydrogels are commonly used for bone tissue engineering, with a number of studies demonstrating the bone regeneration potential of RGD functionalized and γ-irradiated alginate (*30*–*33*), making it a promising base bioink for the 3D bioprinting of osteogenic implants. However, one drawback to using RGD γ-irradiated alginate as a bioink is its low viscosity. It is imperative when printing multilayered structures that the bioink have appropriate rheological properties to prevent collapsing or sagging of the printed structure. The addition of methylcellulose to alginate-based bioinks was found to have a significant effect on both printability and the rate of growth factor release. The addition of methylcellulose has previously been shown to substantially increase the print fidelity of an alginate base bioink (*22*, *34*, *35*), although typically using higher concentrations than the one used in this study. Adding methylcellulose also accelerated the rate of growth factor release. This was previously seen with albumin release from alginate-methylcellulose beads (*36*). Such a polymeric network is at least partially defined by physical entanglements between the alginate or methylcellulose chains. As methylcellulose is characterized by high swellability, when the alginate/methylcellulose bioink is exposed to the medium, it swells rapidly, resulting in

accelerated growth factor release from the bioink. The addition of methylcellulose may also have neutralized the charge on the alginate, which would also influence growth factor release kinetics. In contrast, the addition of nanoparticles, and, in particular, laponite, slowed the release of growth factor from the inks. Both nHA and laponite have previously been shown to facilitate with the adsorption and immobilization of VEGF within a hydrogel due to the strong attraction between the nanoparticles and the growth factor (*21*–*23*). The stronger association between growth factors and laponite can be linked to the physiochemical properties of these particles (*22*, *29*). These disc-shaped particles [typically 25 nm in diameter and 1 nm in thickness (*37*)] are characterized by a highly negatively charged face and a positively charged rim (*22*), with a zeta potential of −61 mV (as determined by the manufacturer). This allowed the positively charged growth factors such as VEGF to form strong electrostatic bonds with the negatively charged face of the nanoparticles (*22*). In contrast, the nHA nanoparticles used in this study, which we have previously shown to have a zeta potential of around −5 mV (*38*), would form a slightly weaker electrostatic bond with the VEGF. The addition of laponite to bioinks has also previously been shown to influence their mechanical properties (*37*). While we did not directly assess whether the addition of laponite influenced the stiffness of our ink, we did observe that it had no effect on their degradability, and on the basis of w/w ratio used in this study, we do not believe it had marked effects on mechanical properties such as matrix stiffness. Previous studies have shown that when using high concentrations of alginate (similar to that used in this study), the addition of laponite does not markedly affect the rheological properties of the bioink (*37*). However, future studies should investigate the overall mechanical properties of a bioink, as this may also influence its osteogenic potential (*39*). A potential limitation of laponite is that the strong electrostatic bond can limit the amount of growth factor released from a delivery system in the short-medium term (*22*). In this study, by tuning the ratio of laponite to alginate, it was possible to engineer bioinks that released most of their loaded protein over 35 days. Therefore, using specifically selected nanoparticles, it is possible to develop bioinks that support growth factor release profiles spanning days to weeks.

Using multiple-tool biofabrication, we demonstrated that distinct growth factor gradients can be established and maintained over time and that incorporating these gradients into printed implants can enhance sprouting angiogenesis in vivo. The process of sprouting angiogenesis begins with the selection of a distinct site on the mother vessel where sprout formation is initiated. This distinct site is referred to as the "tip cell," and as the new sprout elongates, branches, and connects with other sprouts, the selection process for the tip cell is constantly reiterated (*40*). Previous studies have shown in the early postnatal retinas that tip cell migration depends on a gradient of VEGF-A and its proliferation is regulated by its concentration (*40*, *41*). Therefore, the increase in vessel infiltration observed in VEGF gradient implants can possibly be attributed to tip cell migration and proliferation toward the areas of high VEGF concentration (*40*, *41*). In contrast, when VEGF was homogenously distributed within the implant, there was less of a chemotactic effect, resulting in lower levels of vessel infiltration into the center of the construct.

When this bioprinting strategy was used to deliver both growth factors within a large bone defect, there was a significant increase in vessel infiltration within implants containing both a VEGF gradient and BMP-2 compared to those containing VEGF alone. Although it has been shown that delivery of BMP-2 alone can enhance new blood vessel formation within bone defects (*42*, *43*), previous studies have not reported a benefit to delivering both growth factors to the defect site (*17*, *18*). The finding that the laponite-functionalized bioink around the periphery of the implant was slowing the release of VEGF from the implant may partially explain the higher levels of vessel infiltration observed within the composite implant, with the slower VEGF release profile being perhaps more conducive to angiogenesis within the orthotopic environment. Somewhat unexpectedly, despite enhancing overall levels of bone formation, VEGF delivery alone did not increase early vessel infiltration into the implant. Note that orthotopic hematomas, generated by the surgical procedure, would have provided all defects with a source of endogenous chemotactic, angiogenic, and mitogenic growth factors (*17*). This may have mitigated the effect that an implant containing a VEGF gradient alone had on early angiogenesis.

3D printed implants containing spatial gradients of VEGF, coupled with defined BMP-2 localization, enhanced large bone defect healing with little heterotopic bone formation. Critically, this increase in bone healing was achieved using very low concentrations of exogenous growth factors. The concentration of VEGF used in this study was substantially less (80 to 160 times less) than previous studies (*17*, *18*). Achieving therapeutic benefits with these low concentrations of growth factors is important for multiple reasons, not least of which is the observation that high concentrations of VEGF have been previously shown to disrupt osteogenesis as the result of abnormal angiogenesis and vascular structure (*8*). Furthermore, the concentrations of BMP-2 used here are at least an order of magnitude lower than that used previously to repair similar sized defects in a rat femoral defect model (*28*, *31*). Repair in these studies is typically associated with a substantial amount of heterotopic bone formation (*28*, *31*). Directly comparing to previous work in our lab, which used a clinically relevant BMP-2 dose in the same defect model (*28*), the results from this study exhibited substantially less heterotrophic bone formation [10% versus 50% (*28*) of total bone volume]. Although we did not observe full bone bridging after 12 weeks, new bone was still being formed via the process of endochondral ossification at 12 weeks, suggesting that regeneration was still proceeding. Allowing some level of physiological loading earlier in the healing process would likely have further accelerated regeneration (*44*). Together, the results from this study demonstrate the potential of 3D printing morphogen gradients for controlled tissue regeneration (with minimal heterotopic bone formation) without the need of supraphysiological dosages.

The translation of tissue engineering concepts from bench to bedside is a challenging, expensive, and time-consuming process. Numerous products have not made it past phase 2 trials, as they have not shown the expected benefit in patients (*1*, *2*), while others have been associated with marked adverse effects (*3*–*5*). Here, we describe a previously unidentified approach for spatiotemporally defined growth factor delivery and demonstrate a potential clinical utility in the regeneration of large bone defects or the increased vascularization of any 3D printed construct. Proof-of-concept studies in small animals established the potential of these growth factor loaded bioinks for inducing enhanced angiogenesis and bone regeneration without the need for supraphysiological dosages. The benefit of this precise localization of growth factors in both time and space is that it allows for tightly controlled angiogenesis and new tissue formation, thereby reducing off-target effects. It is envisioned that this platform technology could be applied to the controlled regeneration of numerous different tissue types.

MATERIALS AND METHODS

Study design

This study was designed to test whether the delayed release of BMP-2 from bioprinted constructs containing spatial gradients in VEGF will first enhance vascularization and sequentially enhance orthotopic bone regeneration. All animal experiments were conducted in accordance with the recommendations and guidelines of The Health Products Regulatory Authority, the competent authority in Ireland responsible for the implementation of Directive 2010/63/EU on the protection of animals used for scientific purposes in accordance with the requirements of the Statutory Instrument no. 543 of 2012. Subcutaneous mouse experiments were carried out under license (AE 19136/P069), and the rat femoral defect experiments were carried out under license (AE19136/P087) approved by The Health Products Regulatory Authority and in accordance with protocols approved by the Trinity College Dublin Animal Research Ethics Committee. The *n* for rodent models were based on the predicted variance in the model and was powered to detect 0.05 significance. For the subcutaneous surgeries, constructs were implanted in a balanced manner, such that each group contained an implant placed at each of the subcutaneous locations and samples for both surgical procedures were randomly distributed across the operated animals. For the rat surgeries, three rats from the empty group died from unforeseen complications and so were removed from the *n* number at the 12-week time point. One rat from the BMP-2 gradient group at 12-week time point was also removed, as it was deemed a statistical outlier using the Grubbs' test.

Preparation of bioinks

Low–molecular weight sodium alginate (58,000 g/mol) was prepared by irradiating sodium alginate (196, 000 g/mol; Protanal LF 20/40, Pronova Biopolymers, Oslo, Norway) at a gamma dose of 50,000 gray, as previously described (*45*). RGD-modified alginate was prepared by coupling the GGGGRGDSP to the alginate using standard carbodiimide chemistry. All bioinks were prepared by dissolving the RGD γ-irradiated alginate in growth medium, which consisted of alpha minimum essential medium (αMEM) (GlutaMAX; Gibco, Biosciences, Ireland), 10% fetal bovine serum (FBS) (EU Thermo Fisher Scientific), penicillin (100 U/ml; Sigma-Aldrich), and streptomycin (100 g/ml; Sigma-Aldrich) (pen-strep) to make up a final concentration of 3.5% (w/v).

Evaluation of the printability of the bioinks

3D bioplotter from RegenHU (3DDiscovery) was used to evaluate the printability of the generated bioinks. The printability of varying the w/w ratio (2:1, 1:1, and 1:2) of methylcellulose to alginate was evaluated by measuring the spreading ratio as previously described (*39*)

$$\text{Spreading Ratio} = \frac{\text{Printed Filament Diameter}}{\text{Actual Needle Diameter}}$$

Tailoring the growth factor release profile of the vascular bioink

To establish whether increasing the viscosity of the bioink influences growth factor release, methylcellulose (Sigma-Aldrich) was also added at ratio of 1:2 (w/w) to a 3.5% alginate solution of RGD γ-irradiated alginate. To establish whether the addition of clay-based particles to the bioink could further tailor the growth factor release profile of the bioinks, a 3.5% RGD γ-irradiated alginate solution was made, and either methylcellulose (2:1) (w/w) or a combination of both methylcellulose and laponite (Laponite XLG, BYK Additives & Instruments, UK) (6:3:1) (w/w) was added.

To establish whether the addition of nHA to the alginate would facilitate the adsorption and immobilization of growth factors within the hydrogel due to their strong electrostatic attraction between nHAs, three bioinks were tested (*21*). nHAs were prepared following a previously described protocol (*46*). A 3.5% RGD γ-irradiated alginate solution was made, and either methylcellulose (1:2) (w/w) or a combination of methylcellulose and nHA (2:1:2) (w/w) particles was added.

For all the growth factor release studies, VEGF (100 ng/ml; Gibco Life Technologies, Gaithersburg, MD, USA) was added to the solutions using dual-syringe approach, before precross-linking with 60 mM $CaSO_4$ to make the bioinks as previously described (*39*). All constructs were cultured in growth medium in normoxic conditions, and media from each sample were changed bi-weekly. For VEGF release study, medium samples were taken (days 0, 3, 5, and 10) and snap-frozen at −80°C. Hydrogels were also snap-frozen at −80°C on day 0 to quantify the concentration of growth factor present in the constructs directly after printing.

Generation of VEGF gradients using vascular bioink

To demonstrate the utility of the vascular bioink, two strategies were compared to print implants containing a spatial gradient of VEGF. The vascular bioink was prepared, cross-linked with 60 mM $CaSO_4$, and printed to generate three experimental groups: (i) Homogenous VEGF. Bioink loaded with VEGF (100 ng/ml) was used to print constructs 8 mm in diameter and 4 mm high. (ii) Gradient 1. Bioink loaded with VEGF (100 ng/ml) was used to print a central 5-mm core with a VEGF-free bioink printed around the periphery of the 8-mm-diameter construct. (iii) Gradient 2. VEGF (80 ng/ml) was printed into the core, and VEGF (20 ng/ml) was printed into the periphery. Postprinting constructs were cross-linked again in a bath of 100 mM $CaCl_2$ for 1 min. Constructs were cultured in growth medium in normoxic conditions for 14 days in vitro. The center and periphery of each construct were separated by coring out the center from the periphery of the scaffold and then snap-frozen at −80°C, 1 hour after printing, and after 14 days in vitro.

Tailoring the growth factor release profile of the osteoinductive bioink

To investigate whether the addition of laponite can tailor the growth factor release profile over a long culture period, a base bioink (Fast BMP-2 Release) and a laponite bioink (Slow BMP-2 Release) were compared. For both growth factor release profiles, a dual-syringe approach was used to deliver BMP-2 (200 ng/ml; PeproTech, UK) to the solutions before precross-linking with 60 mM $CaSO_4$ to make the bioinks. These were printed into a 100 mM $CaCl_2$ soak agarose mold to generate final constructs of Ø 6 mm by 6 mm high. In addition to comparing the growth factor release profile of the two bioinks, the degradation rate of the bioinks was also investigated. These scaffolds were cultured in normoxic conditions for up to 35 days and media from each sample were changed weekly. For BMP-2 release study, medium samples were taken (days 0, 5, 7, 14, 21, and 35) and snap-frozen at −80°C. Printed hydrogels were also snap-frozen at −80°C on day 0 to quantify the concentration of growth factor present in the constructs directly after printing. For the degradation study, samples were washed and snap-frozen at −80°C and each time point (days 0, 5, 7, 14, and 21). Samples were lyophilized by placing the samples in

a freeze dryer (FreeZone Triad, Labconco, Kansas City, USA). Each sample was then weighed using an analytical balance (Mettler Toledo, XS205).

Enzyme-linked immunosorbent assays

An enzyme-linked immunosorbent assay was used to quantify the levels of VEGF and BMP-2 (Bio-Techne, MN, USA) released by the alginates. The alginate samples were depolymerized with 1 ml of citrate buffer (150 mM sodium chloride, 55 mM sodium citrate, and 20 mM EDTA in H_2O) for 15 min at 37°C. The cell culture media and depolymerized alginate samples were analyzed at the specific time points detailed above. Assays were carried out as per the manufacturer's protocol and analyzed on a microplate reader at a wavelength of 450 nm.

Cell isolation, expansion, and seeding

BMSCs were obtained from the femur of a 4-month-old porcine donor as previously described (*47*). All expansion was conducted in normoxic conditions, expanded in growth medium where the medium was changed twice weekly. Cells were used at the end of passage 3.

Construct design and 3D printing process

A 3D bioplotter from RegenHU (3DDiscovery) was used to print all of the scaffolds. Using a 30-gauge needle, constructs of Ø 4 mm × 5 mm high with both lateral and horizontal porosity and a fiber spacing of 1.2 mm were printed with PCL (Cappa, Perstop). The printing parameters of the PCL were as follows: temperature of thermopolymer tank (69°C), temperature of thermopolymer head (72°C), pressure (1 bar), screw speed (30 rpm), and feed rate (3 mm/s). Scaffolds were sterilized using ethylene oxide sterilization before hydrogel printing.

For the VEGF gradient study, the vascular bioink was prepared, cross-linked with 60 mM $CaSO_4$, and printed within the PCL framework to generate three experimental groups: (i) No VEGF, bioink not loaded with VEGF; (ii) Homogenous, bioink loaded with VEGF (100 ng/ml) deposited (25 ng per construct) throughout the construct; and (iii) Gradient, bioink loaded with VEGF (500 ng/ml) deposited in the center (25 ng per construct) and VEGF-free bioink deposited on the outside (see Fig. 1A). Postprinting constructs were cross-linked again in a bath of 100 mM $CaCl_2$ for 1 min.

For the BMP-2 release study, both a fast and slow release bioink were prepared and using the dual syringe approach, porcine MSCs were (2×10^6/ml) mixed to both bioinks to have an overall seeding density of 500×10^5 porcine MSCs/construct before being cross-linked with 60 mM $CaSO_4$. Both bioinks were printed within the PCL framework to generate two experimental groups: (i) Fast release, fast release bioink loaded with BMP-2 (2 μg/ml; 0.5 μg per construct) deposited only in the periphery with the fast release bioink not loaded with BMP-2 in the center; and (ii) Slow release, slow release bioink loaded with BMP-2 (2 μg/ml; 0.5 μg per construct) deposited only in the periphery with the fast release bioink not loaded with BMP-2 in the center (see Fig. 2A). Postprinting constructs were cross-linked again in a bath of 100 mM $CaCl_2$ for 1 min.

For the rat femoral defect, the vascular bioink, the osteoinductive bioink, and a base bioink (3.5% RGD γ-irradiated alginate and 1.75% methylcellulose) were prepared, cross-linked with 60 mM $CaSO_4$, and printed within the PCL framework to generate three experimental groups: (i) VEGF Gradient, the vascular bioink loaded with VEGF (500 ng/ml) in the center of the implant and base bioink in the periphery; (ii) BMP-2 gradient, the osteoinductive bioink loaded with BMP-2 (10 μg/ml) in the implant periphery (2 μg per construct), with the base bioink in the center; and (iii) Composite (VEGF+BMP-2), the osteoinductive bioink in the periphery with the vascular bioink in the center (see Fig. 3A). Postprinting constructs were cross-linked again in a bath of 100 mM $CaCl_2$ for 1 min.

Animals and surgical procedures

Subcutaneous surgeries were performed on 20 8-week-old female BALB/c OlaHsd-Foxn 1nu nude mice (12 mice for the VEGF gradient study and 8 for the BMP-2 gradient study) (Envigo, Oxon, UK) as previously described (*47*). Scaffolds were 3D printed the morning of surgeries and implanted that day. Constructs were implanted in a balanced manner, such that each group contained an implant placed at each of the two subcutaneous locations and samples were randomly distributed across the operated animals.

For the rat segmental surgery, 72 12-week-old F344 Fischer male rats (Envigo, Oxon, UK) were anesthetized in an induction box using a mix of isoflurane and oxygen, initially at a flow rate of isoflurane of 5 liters/min to induce, followed by ~3 liters/min to maintain anesthesia. Once anesthetized, the animal was transferred to a heating plate that was preheated to 37°C and preoperative analgesia was provided by buprenorphine (0.03 mg/ml). Surgical access to the femur was achieved via an anterolateral longitudinal skin incision and separation of the hindlimb muscles, the vastus lateralis, and biceps femoris. The femoral diaphysis was exposed by circumferential elevation of attached muscles, and the periosteum was removed. Before the creation of the defect, a PEEK plate was fixed to the anterolateral femur and was held in position using a clamp. Holes were created in the femur with a surgical drill using the plate as a template. Screws were then inserted into the drill holes in the femur to maintain the fixation plate in position. A 5-mm segmental defect was created using an oscillating surgical saw under constant irrigation with sterile saline solution. In the test groups, a scaffold was placed in the defect after a thorough washout of the surgical site. In the case of the empty defect group, the gap between bone ends was left empty. Soft tissue was accurately readapted with absorbable suture material. Closure of the skin wound was achieved using suture material and tissue glue.

μCT imaging

Eight weeks after surgery, the BMP-2 gradient scaffolds were extracted and incubated in paraformaldehyde for 24 hours before being imaged via μCT scans on a MicroCT42 (Scanco Medical, Brüttisellen, Switzerland) as previously described (*47*).

Vascular-CT imaging

Two weeks after surgery, 24 rats underwent a vascular perfusion protocol developed by Daly *et al.* (*28*). Briefly, the rat was sacrificed using CO_2 asphyxiation, and the thoracic cavity was opened to insert a 20-gauge needle through the left ventricle of the heart. The inferior cava was cut and solutions of heparin (25 U/ml), and then, phosphate-buffered saline (PBS) was perfused through the vasculature using a peristaltic pump (Masterflex, Cole-Parmer, Vernon Hills, IL, USA) until the vasculature system was completely flushed clear. A solution of 10% formalin was then perfused for 5 min. Animals received a final perfusion of 20- to 25-ml radiopaque contrast agent MICROFIL (Flow Tech, Carver, MA, USA) and were left at 4°C overnight. Explants were extracted and incubated in PBS for 24 hours before being imaged via μCT scans on a MicroCT42 (Scanco Medical,

Brüttisellen, Switzerland) at 70 kVp, 113 μA, and a 10-μm voxel size. The volume of interest (VOI) was determined by positioning a 5-mm circle around the cross section of the femur with an overall length of 6.26 mm. MICROFIL has the same threshold as bone mineral, and therefore, to segment perfused vasculature from mineralized tissue within each construct, two scans were analyzed: calcified construct versus decalcified construct. The calcified constructs were scanned and postprocessed using a threshold value that accurately depicted both the mineral content and the vessel volume by visual inspection of the 2D grayscale tomograms (Scanco Medical MicroCT42). Noise was removed using a low-pass Gaussian filter (sigma = 1.2, support = 2), and a global threshold of 210 was applied. Next, samples were decalcified in EDTA (15 weight %, pH 7.4) for 2 weeks with the decalcification solution replaced daily (decalcified constructs). After 2 weeks, these decalcified constructs were scanned using the same settings and postprocessed at the same threshold as the calcified constructs to determine mineral content. Mineralized tissue content was determined by subtracting the bone volume of the decalcified scans from the calcified scans. Next, the decalcified scans were postprocessed at a threshold of 99 that accurately depicted just the vessel volume upon visual inspection of the 2D grayscale tomograms.

In vivo μCT imaging

μCT scans were performed on the rats using a Scanco Medical vivaCT 80 system (Scanco Medical, Bassersdorf, Switzerland). Rats (n = 9) were scanned at 4, 8, 10, and 12 weeks after surgery to assess defect bridging and bone formation within the defect. First, anesthesia was induced in an induction box using a mix of isoflurane and oxygen, initially at a flow rate of isoflurane of 5 liters/min to induce, followed by ~3 liters/min to maintain anesthesia. Next, the rats were placed inside the vivaCT scanner, and anesthesia was maintained by isoflurane-oxygen throughout the scan. Next, a radiographic scan of the whole animal was used to isolate the rat femur. The animal's femur was aligned parallel to the scanning field of view to simplify the bone volume assessments. Scans were performed using a voltage of 70 kVp and a current of 113 μA. A Gaussian filter (sigma = 0.8, support = 1) was used to suppress noise, and a global threshold of 210 was applied. A voxel resolution of 35 μm was used throughout. 3D evaluation was carried out on the segmented images to determine bone volume and density and to reconstruct a 3D image. Bone volume and bone density in the defects were quantified by measuring the total quantity of mineral in the central 130 slices of the defect. To differentiate regional differences in bone formation, three VOIs were created. Concentric Ø2 mm, Ø4 mm, and Ø10 mm were aligned with the defect and used to encompass bone formation. The VOIs were aligned using untreated native bone along the femur. The core bone volume was quantified from the inner Ø2-mm VOI. The annular bone volume was quantified by subtracting the Ø2-mm VOI from the Ø4-mm VOI. Ectopic bone volume was quantified by subtracting the Ø4-mm VOI from the Ø10-mm VOI. The bone volume percentages for each region were then calculated by dividing the corresponding bone volume (i.e., bone volume in the annulus) by the total bone volume in the defect. The bone volume and densities were then quantified using scripts provided by Scanco.

Histological analysis

For segmental defect samples, all constructs that were not being processed for vascular-CT imaging, were decalcified in Decalcifying Solution-Lite (Sigma-Aldrich) for 1 week before tissue processing. Once decalcified, all samples were dehydrated and embedded in paraffin using an automatic tissue processor (Leica ASP300, Leica). All samples were sectioned with a thickness of 8 μm using a rotary microtome (Leica Microtome RM2235, Leica). Sections were stained with H&E for vessel infiltration, Safranin O to assess sulphated glycosaminoglycans (sGAG) content, and Goldner's trichrome for bone formation. Quantitative analysis was performed on multiple H&E-stained slices, whereby vessels (positive staining for endothelium and erythrocytes present within the lumen), were counted on separate sections taken throughout each construct and averaged for each construct. Safranin O sections were evaluated for new developing bone (positive sGAG content). Masson's trichrome–stained sections were evaluated for new bone formation. The percentage of developing bone, new bone, and marrow per total area of construct was measured in separate sections with the Deconvolution ImageJ plugin.

Immunofluorescence analysis

Immunofluorescence analysis was used to detect α-SMA and vWF as previously described (*47*). Briefly, following blocking step, sections were then incubated overnight at +4°C with goat polyclonal α-SMA (1:250; ab21027, Abcam) in PBS with 3% of donkey serum (w/v) and 1% bovine serum albumin (BSA). After three washing steps with PBS containing 1% w/v BSA, the sections were incubated with Alexa Fluor 488 donkey anti-goat secondary antibody (1:200; ab150129, Abcam) for 1 hour at room temperature in the dark. The samples were washed three times in PBS with 1% w/v BSA, and the slides were then incubated overnight at +4°C with rabbit polyclonal vWF antibody (1:200; ab6994, Abcam) in PBS with 3% of donkey serum (w/v) and 1% BSA (all from Sigma-Aldrich). After three washing steps with PBS and 1% w/v BSA, the sections were incubated with Alexa Fluor 647 donkey anti-rabbit secondary antibody (1:200; ab150075, Abcam) for 1 hour at room temperature in the dark. Last, samples were washed three times with PBS and 1% w/v BSA, and the sections were mounted using 4′,6-diamidino-2-phenylindole mounting media (Sigma-Aldrich). Fluorescence emission was detected using a confocal laser scanning microscopy (Olympus FluoView 1000).

Statistical analysis

Results were expressed as means ± SD. Statistics was performed using the following variables: (i) When there were two groups and one time point, a standard two-tailed t test was performed. (ii) When there were more than two groups and one time point, a one-way analysis of variance (ANOVA) was performed. (iii) When there were more than two groups and multiple time points, a two-way ANOVA was performed. All analyses were performed using GraphPad (GraphPad Software, La Jolla, CA, USA; www.graphpad.com). For all comparisons, the level of significance was $P \leq 0.05$.

SUPPLEMENTARY MATERIALS

Supplementary material for this article is available at http://advances.sciencemag.org/cgi/content/full/6/33/eabb5093/DC1

View/request a protocol for this paper from *Bio-protocol*.

REFERENCES AND NOTES

1. M. Simons, J. A. Ware, Therapeutic angiogenesis in cardiovascular disease. *Nat. Rev. Drug Discov.* **2**, 863–871 (2003).
2. T. D. Henry, B. H. Annex, G. McKendall, M. A. Azrin, J. J. Lopez, F. J. Giordano, P. K. Shah, J. T. Willerson, R. L. Benza, D. S. Berman, C. M. Gibson, A. Bajamonde, A. C. Rundle, J. Fine,

E. McCluskey; VIVA Investigators, The VIVA trial: Vascular endothelial growth factor in ischemia for vascular angiogenesis. *Circulation* **107**, 1359–1365 (2003).
3. N. E. Epstein, Complications due to the use of BMP/INFUSE in spine surgery: The evidence continues to mount. *Surg. Neurol. Int.* **4**, S343–S352 (2013).
4. L. B. E. Shields, G. H. Raque, S. D. Glassman, M. Campbell, T. Vitaz, J. Harpring, C. B. Shields, Adverse effects associated with high-dose recombinant human bone morphogenetic protein-2 use in anterior cervical spine fusion. *Spine* **31**, 542–547 (2006).
5. K. Lee, E. A. Silva, D. J. Mooney, Growth factor delivery-based tissue engineering: General approaches and a review of recent developments. *J. R. Soc. Interface* **8**, 153–170 (2011).
6. H. Uludag, D. D'Augusta, R. Palmer, G. Timony, J. Wozney, Characterization of rhBMP-2 pharmacokinetics implanted with biomaterial carriers in the rat ectopic model. *J. Biomed. Mater. Res.* **46**, 193–202 (1999).
7. P. J. Bouletreau, S. M. Warren, J. A. Spector, Z. M. Peled, R. P. Gerrets, J. A. Greenwald, M. T. Longaker, Hypoxia and VEGF up-regulate BMP-2 mRNA and protein expression in microvascular endothelial cells: Implications for fracture healing. *Plast. Reconstr. Surg.* **109**, 2384–2397 (2002).
8. C. Liu, A. B. Castillo, Targeting osteogenesis-angiogenesis coupling for bone repair. *J. Am. Acad. Orthop. Surg.* **26**, e153–e155 (2018).
9. R. A. Carano, E. H. Filvaroff, Angiogenesis and bone repair. *Drug Discov. Today* **8**, 980–989 (2003).
10. C. Maes, P. Carmeliet, K. Moermans, I. Stockmans, N. Smets, D. Collen, R. Bouillon, G. Carmeliet, Impaired angiogenesis and endochondral bone formation in mice lacking the vascular endothelial growth factor isoforms VEGF164 and VEGF188. *Mech. Dev.* **111**, 61–73 (2002).
11. J. Street, M. Bao, L. deGuzman, S. Bunting, F. V. Peale, N. Ferrara, H. Steinmetz, J. Hoeffel, J. L. Cleland, A. Daugherty, N. van Bruggen, H. P. Redmond, R. A. D. Carano, E. H. Filvaroff, Vascular endothelial growth factor stimulates bone repair by promoting angiogenesis and bone turnover. *Proc. Natl. Acad. Sci. U.S.A.* **99**, 9656–9661 (2002).
12. E. Zelzer, W. McLean, Y. S. Ng, N. Fukai, A. M. Reginato, S. Lovejoy, P. A. D'Amore, B. R. Olsen, Skeletal defects in VEGF(120/120) mice reveal multiple roles for VEGF in skeletogenesis. *Development* **129**, 1893–1904 (2002).
13. Z. S. Patel, S. Young, Y. Tabata, J. A. Jansen, M. E. K. Wong, A. G. Mikos, Dual delivery of an angiogenic and an osteogenic growth factor for bone regeneration in a critical size defect model. *Bone* **43**, 931–940 (2008).
14. H. R. Peng, A. Usas, A. Olshanski, A. M. Ho, B. Gearhart, G. M. Cooper, J. Huard, VEGF improves, whereas sFlt1 inhibits, BMP2-induced bone formation and bone healing through modulation of angiogenesis. *J. Bone Miner. Res.* **20**, 2017–2027 (2005).
15. J. M. Kanczler, P. J. Ginty, L. White, N. M. P. Clarke, S. M. Howdle, K. M. Shakesheff, R. O. C. Oreffo, The effect of the delivery of vascular endothelial growth factor and bone morphogenic protein-2 to osteoprogenitor cell populations on bone formation. *Biomaterials* **31**, 1242–1250 (2010).
16. S. Zhang, J. Chen, Y. Yu, K. Dai, J. Wang, C. Liu, Accelerated bone regenerative efficiency by regulating sequential release of BMP-2 and VEGF and synergism with sulfated chitosan. *ACS Biomater Sci. Eng.* **5**, 1944–1955 (2019).
17. D. H. R. Kempen, L. Lu, A. Heijink, T. E. Hefferan, L. B. Creemers, A. Maran, M. J. Yaszemski, W. J. A. Dhert, Effect of local sequential VEGF and BMP-2 delivery on ectopic and orthotopic bone regeneration. *Biomaterials* **30**, 2816–2825 (2009).
18. R. E. Geuze, L. F. H. Theyse, D. H. R. Kempen, H. A. W. Hazewinkel, H. Y. A. Kraak, F. C. Öner, W. J. A. Dhert, J. Alblas, A differential effect of bone morphogenetic protein-2 and vascular endothelial growth factor release timing on osteogenesis at ectopic and orthotopic sites in a large-animal model. *Tissue Eng. Part A* **18**, 2052–2062 (2012).
19. T. Pufe, B. Wildemann, W. Petersen, R. Mentlein, M. Raschke, G. Schmidmaier, Quantitative measurement of the splice variants 120 and 164 of the angiogenic peptide vascular endothelial growth factor in the time flow of fracture healing: A study in the rat. *Cell Tissue Res.* **309**, 387–392 (2002).
20. S. Uchida, A. Sakai, H. Kudo, H. Otomo, M. Watanuki, M. Tanaka, M. Nagashima, T. Nakamura, Vascular endothelial growth factor is expressed along with its receptors during the healing process of bone and bone marrow after drill-hole injury in rats. *Bone* **32**, 491–501 (2003).
21. Y. Chen, J. Wang, X. Zhu, Y. Fan, X. Zhang, Adsorption and release behaviors of vascular endothelial growth factor on porous hydroxyapatite ceramic under competitive conditions. *J. Biomater. Tissue Eng.* **4**, 155–161 (2014).
22. T. Ahlfeld, G. Cidonio, D. Kilian, S. Duin, A. R. Akkineni, J. I. Dawson, S. Yang, A. Lode, R. O. C. Oreffo, M. Gelinsky, Development of a clay based bioink for 3D cell printing for skeletal application. *Biofabrication* **9**, 034103 (2017).
23. J. I. Dawson, J. M. Kanczler, X. B. Yang, G. S. Attard, R. O. Oreffo, Clay gels for the delivery of regenerative microenvironments. *Adv. Mater.* **23**, 3304–3308 (2011).
24. A. Shamloo, N. Ma, M. M. Poo, L. L. Sohn, S. C. Heilshorn, Endothelial cell polarization and chemotaxis in a microfluidic device. *Lab Chip* **8**, 1292–1299 (2008).
25. A. Shamloo, S. C. Heilshorn, Matrix density mediates polarization and lumen formation of endothelial sprouts in VEGF gradients. *Lab Chip* **10**, 3061–3068 (2010).
26. Y. Aizawa, R. Wylie, M. Shoichet, Endothelial cell guidance in 3D patterned scaffolds. *Adv. Mater.* **22**, 4831–4835 (2010).
27. D. Odedra, L. L. Y. Chiu, M. Shoichet, M. Radisic, Endothelial cells guided by immobilized gradients of vascular endothelial growth factor on porous collagen scaffolds. *Acta Biomater.* **7**, 3027–3035 (2011).
28. A. C. Daly, P. Pitacco, J. Nulty, G. M. Cunniffe, D. J. Kelly, 3D printed microchannel networks to direct vascularisation during endochondral bone repair. *Biomaterials* **162**, 34–46 (2018).
29. D. M. R. Gibbs, C. R. M. Black, G. Hulsart-Billstrom, P. Shi, E. Scarpa, R. O. C. Oreffo, J. I. Dawson, Bone induction at physiological doses of BMP through localization by clay nanoparticle gels. *Biomaterials* **99**, 16–23 (2016).
30. E. Alsberg, H. J. Kong, Y. Hirano, M. K. Smith, A. Albeiruti, D. J. Mooney, Regulating bone formation via controlled scaffold degradation. *J. Dent. Res.* **82**, 903–908 (2016).
31. Y. M. Kolambkar, K. M. Dupont, J. D. Boerckel, N. Huebsch, D. J. Mooney, D. W. Hutmacher, R. E. Guldberg, An alginate-based hybrid system for growth factor delivery in the functional repair of large bone defects. *Biomaterials* **32**, 65–74 (2011).
32. Y. M. Kolambkar, J. D. Boerckel, K. M. Dupont, M. Bajin, N. Huebsch, D. J. Mooney, D. W. Hutmacher, R. E. Guldberg, Spatiotemporal delivery of bone morphogenetic protein enhances functional repair of segmental bone defects. *Bone* **49**, 485–492 (2011).
33. J. D. Boerckel, Y. M. Kolambkar, K. M. Dupont, B. A. Uhrig, E. A. Phelps, H. Y. Stevens, A. J. García, R. E. Guldberg, Effects of protein dose and delivery system on BMP-mediated bone regeneration. *Biomaterials* **32**, 5241–5251 (2011).
34. K. Schütz, A.-M. Placht, B. Paul, S. Brüggemeier, M. Gelinsky, A. Lode, Three-dimensional plotting of a cell-laden alginate/methylcellulose blend: Towards biofabrication of tissue engineering constructs with clinically relevant dimensions. *J. Tissue Eng. Regen. Med.* **11**, 1574–1587 (2017).
35. K. Markstedt, A. Mantas, I. Tournier, H. Martínez Ávila, D. Hägg, P. Gatenholm, 3D bioprinting human chondrocytes with nanocellulose-alginate bioink for cartilage tissue engineering applications. *Biomacromolecules* **16**, 1489–1496 (2015).
36. A. Nochos, D. Douroumis, N. Bouropoulos, In vitro release of bovine serum albumin from alginate/HPMC hydrogel beads. *Carbohydr. Polym.* **74**, 451–457 (2008).
37. J. L. Dávila, M. A. d'Ávila, Rheological evaluation of Laponite/alginate inks for 3D extrusion-based printing. *Int. J. Adv. Manuf. Technol.* **101**, 675–686 (2019).
38. T. Gonzalez-Fernandez, B. N. Sathy, C. Hobbs, G. M. Cunniffe, H. O. McCarthy, N. J. Dunne, V. Nicolosi, F. J. O'Brien, D. J. Kelly, Mesenchymal stem cell fate following non-viral gene transfection strongly depends on the choice of delivery vector. *Acta Biomater.* **55**, 226–238 (2017).
39. F. E. Freeman, D. J. Kelly, Tuning alginate bioink stiffness and composition for controlled growth factor delivery and to spatially direct MSC fate within bioprinted tissues. *Sci. Rep.* **7**, 17042 (2017).
40. H. Gerhardt, VEGF and endothelial guidance in angiogenic sprouting. *Organogenesis* **4**, 241–246 (2008).
41. H. Gerhardt, M. Golding, M. Fruttiger, C. Ruhrberg, A. Lundkvist, A. Abramsson, M. Jeltsch, C. Mitchell, K. Alitalo, D. Shima, C. Betsholtz, VEGF guides angiogenic sprouting utilizing endothelial tip cell filopodia. *J. Cell Biol.* **161**, 1163–1177 (2003).
42. H. B. Pearson, D. E. Mason, C. D. Kegelman, L. Zhao, J. H. Dawahare, M. A. Kacena, J. D. Boerckel, Effects of bone morphogenetic protein-2 on neovascularization during large bone defect regeneration. *Tissue Eng. Part A* **25**, 1623–1634 (2019).
43. E. A. Phelps, A. J. Garcia, Engineering more than a cell: Vascularization strategies in tissue engineering. *Curr. Opin. Biotechnol.* **21**, 704–709 (2010).
44. A. M. McDermott, S. Herberg, D. E. Mason, J. M. Collins, H. B. Pearson, J. H. Dawahare, R. Tang, A. N. Patwa, M. W. Grinstaff, D. J. Kelly, E. Alsberg, J. D. Boerckel, Recapitulating bone development through engineered mesenchymal condensations and mechanical cues for tissue regeneration. *Sci. Transl. Med.* **11**, eaav7756 (2019).
45. O. Jeon, C. Powell, S. M. Ahmed, E. Alsberg, Biodegradable, photocrosslinked alginate hydrogels with independently tailorable physical properties and cell adhesivity. *Tissue Eng. Part A* **16**, 2915–2925 (2010).
46. G. M. Cunniffe *et al.*, The synthesis and characterization of nanophase hydroxyapatite using a novel dispersant-aided precipitation method. *J. Biomed. Mater. Res. A* **95**, 1142–1149 (2010).
47. F. E. Freeman, D. C. Browe, J. Nulty, S. Von Euw, W. L. Grayson, D. J. Kelly, Biofabrication of multiscale bone extracellular matrix scaffolds for bone tissue engineering. *Eur. Cell. Mater.* **38**, 168–187 (2019).

Acknowledgments: We thank the staff at the Bioresources Unit in Trinity College Dublin for veterinary assistance and technical support. **Funding:** This publication has emanated from research supported by a research grant from the European Research Council (ERC) under grant no. 647004, the Irish Research Council (GOIPD/2016/324), and NIH's NIAMS grant R01AR063194. **Author contributions:** F.E.F. was responsible for technical design, development of bioinks, performing all animal surgeries, performing vessel perfusion, all CT scans, data interpretation, histological analysis, and drafting the paper. P.P. assisted with the rat surgeries and assisted with the vessel perfusions. L.H.A.v.D. assisted with CT analyses

and CT scans. J.N. and D.C.B. assisted with all animal surgeries. J.-Y.S. and E.A. developed the RGD γ-irradiated alginate. D.J.K. conceived and helped design the experiments, oversaw the collection of results and data interpretation, and finalized the paper. **Competing interests:** Research undertaken in the laboratory of D.J.K. at Trinity College Dublin is part-funded by Johnson & Johnson. The authors declare no other competing interests. **Data and materials availability:** All data needed to evaluate the conclusions in the paper are present in the paper and/or the Supplementary Materials. Additional data related to this paper may be requested from the authors.

Submitted 28 February 2020
Accepted 2 July 2020
Published 14 August 2020
10.1126/sciadv.abb5093

Citation: F. E. Freeman, P. Pitacco, L. H. A. van Dommelen, J. Nulty, D. C. Browe, J.-Y. Shin, E. Alsberg, D. J. Kelly, 3D bioprinting spatiotemporally defined patterns of growth factors to tightly control tissue regeneration. *Sci. Adv.* **6**, eabb5093 (2020).

3D bioprinting spatiotemporally defined patterns of growth factors to tightly control tissue regeneration

Fiona E. Freeman, Pierluca Pitacco, Lieke H. A. van Dommelen, Jessica Nulty, David C. Browe, Jung-Youn Shin, Eben Alsberg and Daniel J. Kelly

Sci Adv **6** (33), eabb5093.
DOI: 10.1126/sciadv.abb5093